EUROfusion

EUROFUSION WPMST1–PR(15)21

T. Lunt et al.

Optimization of the Snowflake Divertor by Means of EMC3-Eirene Simulations

Preprint of Paper to be submitted for publication in
Plasma Physics and Controlled Fusion

This work has been carried out within the framework of the EUROfusion Consortium and has received funding from the Euratom research and training programme 2014-2018 under grant agreement No 633053. The views and opinions expressed herein do not necessarily reflect those of the European Commission.

Optimization of the snowflake divertor by means of EMC3-Eirene simulations

T. Lunt[1], W.A.J. Vijvers[2], G.P. Canal[2], B.P. Duval[2], Y. Feng[3], B. Labit[2], P. Mc Carthy[4], H. Reimerdes[2], M. Wischmeier[1]

[1]Max Planck Institute for Plasma Physics, Boltzmannstr. 2, 85748 Garching, Germany

[2]Ecole Polytechnique Fédérale de Lausanne, Centre de Recherches en Physique des Plasmas, CH-1015 Lausanne, Switzerland

[3]Max Planck Institute for Plasma Physics, Wendelsteinstr. 1, 17491 Greifswald, Germany

[4]Department of Physics, University College Cork, Cork, Ireland

E-mail: `tilmann.lunt@ipp.mpg.de`

Abstract. In continuation of recent EMC3-Eirene simulations of a series of 'snowflake plus' (SF^+) configurations in TCV [1] we report on simulations with the same code applied to 'snowflake minus' (SF^-) configurations, where the secondary X-point (x_2) is located in the common flux region of the primary separatrix on the low-field side of the primary one. While for the SF^+ the power flux to the secondary strike points (SPs) was only of the order of 1 % in the simulation and $\sim$ 10 % experimentally, a much higher flux was found for the SF^- simulations, consistent with recent measurements [2]. The ratio of total power fluxes P_{SP2}/P_{SP4}, as well as that of the peak values $r_{2/4} = q_{||,max,SP2}/q_{||,max,SP4}$ to the primary and secondary outer SPs (labeled by SP 2 and SP 4), can be tuned by varying the radial magnetic position ρ_{x2} of x_2. A reduction of a factor of two is found for $q_{||,max,SP2}$ for the equal power load, $r_{2/4} = 1$, considered as the optimum at $\rho_{x2} \sim 1.013$, which corresponds to a fraction of the power fall-off length λ_q at the outboard mid-plane. In addition to these pure deuterium simulations discharges with nitrogen- and neon impurities radiating 20 % of the input power are simulated. Due to an impurity accumulation effect between SP 2 and x_2 more power is radiated on the LFS reducing the power load in particular for the outer SPs. Due to the increase of the outboard mid-plane to target connection length of a factor of two the outer target is expected to detach at lower line-integrated densities compared to the single null (SN) configuration. For all these reasons the maximum tolerable P_{sep}/R is expected to be significantly larger in a LFS SF^- compared to a SN.

1. Introduction

The divertor tokamak design in single-null configuration (SN) is presently regarded as one of the most successful concepts to realize a nuclear fusion reactor. In such a configuration, which facilitates access to the high confinement regime (H-Mode) envisaged for a reactor, the plasma is divided into a region with closed magnetic flux

surfaces, the confinement region, and two regions of open field lines, where the first, the common flux region or scrape-off layer (SOL), shares a boundary surface with the confinement region, while the second, the 'private flux region', adjoins the confinement region only at the X-point. The heat produced or absorbed in the confinement region enters the SOL via diffusive or convective radial transport, where parallel heat transport is responsible for guiding a large amount of power to very small areas in the vicinity of the two divertor strike points (SPs). The power flux densities occurring near these locations are close to the limits present day materials can cope with and are expected to become even larger in ractor-sized machines. Fortunately, the problem is strongly relaxed for 'detached' divertor conditions observed at high line integrated plasma densities [3], where a large part of this power is transferred to neutrals, to radiation and/or the far-SOL region. However, it is not certain whether a sufficient degree of detachment can be achieved and if it can be maintained during all phases of the discharge. For this reason, heat exhaust is regarded as one of the most serious problems in fusion research [4].

Experimentally it is observed that the power threshold P_{LH} to enter H-mode depends on the direction of the ion ∇B drift. For the 'forward field' case, i.e. when the ion ∇B drift is directed towards the X-point P_{LH} is significantly lower than for the 'reversed field' case [5, 6]. While in the reversed field configuration only a small asymmetry between the power fluxes to the inner- and outer target is observed, this asymmetry is substantially larger in the forward field case [7] (for a typical power deposition profile cf. Fig. 23 in Ref. [8] or Fig. 6 in Ref. [9]). Additionally, it is observed in devices of the size of ASDEX Upgrade [10, 11] that the inner target reaches detachment at significantly lower plasma densities than the outer one. For this reason, and since ITER and DEMO require a low P_{LH} [12], the *outer* strike point will likely define the limit in maximum tolerable fusion power of the device.

One might expect that the most effective way to reduce the power flux density at the targets is to increase the magnetic flux expansion , i.e. the distance of neighboring SOL flux surfaces in the divertor compared to their upstream distance, which is the principal idea of the recently investigated 'X-divertor' [13]. However, a spreading of the power over a larger poloidal interval on the target can also be achieved by inclining the divertor targets poloidally, which in addition favors a high neutral compression in the divertor by increasing the divertor closure [8, 14]. The combination of these two geometrical measures is limited though by a required minimum field line incidence angle $\theta_\perp$ perpendicular to the target surface as discussed more in detail in Appendix A. A divertor with a high flux expansion will then need to operate at small target inclination angles and will likely require strong neutral gas baffling. Such a design would then resemble that of ASDEX [15] operated in the 1980ies, which was optimized according to these criteria.

The 'snowflake divertor' (SF) [16] was proposed as a concept to solve the heat exhaust problem reducing the maximum heat flux density near the SPs through a series of other mechanisms [17], e.g. the occurrence of two additional SPs. This configuration is

characterized by a second order null-point, where not only the poloidal magnetic field vanishes, but also its first spatial derivatives. Given that it would require an infinitely accurate control of the poloidal field coil currents, an *exact* SF configuration can never be achieved in an experiment. It can, however, be approached by placing a secondary X-point in the vicinity of the primary one. Following the convention introduced by Ryutov (in the generalized form including 'asymmetric' SF configurations) [18] we will refer to a 'snowflake plus' (SF^+) configuration if the secondary X-point is located in the private flux region and a 'snowflake minus' (SF^-) configuration if the secondary X-point is situated in the common flux region (cf. Fig. 1).

Motivated by the assumption that the exact SF would constitute the optimum situation we recently reported on a series of EMC3-Eirene simulations of SF^+ equilibria that approach the exact SF up to a spatial distance between the X-points of $0.01\times a$, where a is the minor radius of the plasma [1]. Assuming a purely diffusive transport with spatially constant coefficients, it was found in the simulations that the power fluxes to the secondary SPs are about 1 % of the total input power P_{in} only, while experimentally 10 % was measured. From this strong discrepancy between the code and the measurements we inferred the occurrence of an enhanced transport across the X-point in the experiment, e.g. driven by the flute-like instabilities predicted by Ryutov [19] occurring at high β_{pol}. Alternatively or additionally, drifts might play an important role in the transport across the separatrix [20]. An inaccuracy of the equilibrium reconstruction is also currently investigated as an alternative explanation. In any case, a redeposition of 10 % of the power to the secondary targets only would hardly justify the challenge of building a reactor in SF configuration, so that this option would only be attractive, if the effect scales with machine size and/or with β_{pol}.

In view of the finding that the power diffusion into the private flux region assuming constant $D_\perp$ and $\chi_\perp$ of typical values in both the SN and the SF^+ configurations is very small, it is actually not surprising that only little power can be re-directed to other SPs. Changing the topology of the common flux region, on the other hand, a much larger re-direction of power can be achieved as also observed in TCV [2]. We will analyze and optimize this configuration in this follow-up article on a series of simulations on SF^- equilibria.

After introducing an alternative set of parameters to characterize the equilibria with a secondary X-point in Sec. 2, comparing the geometrical properties of different configurations in Sec. 3 and describing the construction of a computational grid for EMC3-Eirene in Sec. 4, we will present the simulation results in Sec. 5, discuss the currents in the poloidal field coils required for a SF divertor in Sec. 6 and close with a summary and outlook in Sec. 7. Detailed information on Eirene can be found in Ref. [21] while the working principle, as well as the full set of equations solved by EMC3 and the coupling to Eirene are described in detail in Ref. [22].

2. Characterization of configurations with a secondary X-point

Magnetic equilibria with two X-points can be characterized by the parameters σ and θ, where σ is the spatial distance d_x between X-points normalized to the minor plasma radius a, while θ is the angle between a line connecting the two X-points and a line perpendicular to the segment between the magnetic axis and the primary X-point in the poloidal plane (cf. Fig. 1 left) [18]. Note that in the experiment the two X-points will never have exactly the same poloidal magnetic flux values and so 'primary' always refers to the X-point that lies on the boundary of the confinement region, the 'primary separatrix'. Such geometrical coordinates have certain advantages, e.g. the full and continuous coverage of the parameter space or the direct relation of σ to the poloidal field gradient in the X-point region. However, due to the strong anisotropy of transport in a magnetized plasma, configurations with similar transport properties must not necessarily have the same (σ, θ). Moving the secondary X-point along a flux surface is expected (and will be seen in Sec. 5.2) to have a smaller effect than moving it perpendicularly to this direction. In addition to the (σ, θ) notation this motivates the usage of coordinates (ρ, ϑ) aligned to the magnetic field. The radial position of a point at the poloidal magnetic flux Ψ is specified by $\rho = \left(\left(\Psi - \Psi_o\right) / \left(\Psi_{x1} - \Psi_o\right)\right)^{0.5}$, where Ψ_o is the flux on the magnetic axis and Ψ_{x1} that at the primary X-point, while ϑ is a poloidal variable defined along that flux surface. As illustrated in Fig. 1, ϑ is defined as -2 at the inner target, -0.5 at the inboard mid-plane, 0 at the top, 0.5 at the outboard mid-plane and $+2$ at the outer target. Furthermore, ϑ is equal to ± 1 at the primary X-point on the primary separatrix. Inbetween these reference points ϑ is piecewise linear with the poloidal arc length along a particular surface. Note that for $\rho < 1$ the interval for ϑ between -1 and $+1$ is undefined and that ϑ jumps discontinuously there. For the different ρ_{x2} and ϑ_{x2} positions of the secondary X-point different names are commonly used in the literature that are summarized in Tab. 1.

3. Geometrical considerations comparing the DN and LFS SF$^-$ configurations

Topologically, all configurations with two X-points, $\rho_{x2} > 1$ and ϑ_{x2} between -2 and $+2$ are equal and so in particular also the LFS SF$^-$ and the DN. There is, however, a significant difference between these two configurations illustrated in Fig. 2: In both the DN and the LFS SF$^-$ as well as the SN power is transported radially across the primary separatrix predominantly at the outboard mid-plane and guided via parallel transport to the primary targets in the near SOL region, as illustrated by the thick solid and dashed arrows in Fig. 2. Approaching the secondary separatrix towards the primary one in the DN part of the power that crosses this boundary is redirected from the inner- to the upper target (dashed blue arrows), while the outer target receives the power fluxes from both sides of the secondary separatrix (solid blue arrows). In

ASDEX Upgrade (AUG) in forward field configuration this is advantageous or even counter productive since the upper divertor is an open one and not designed to handle large amounts of power, while the inner divertor is not yet at its limit. In the LFS SF$^-$ case, on the other hand, this redirection of power by the secondary X-point affects the *outer* target. Part of the heat flux that would reach the *outer*, otherwise heavily loaded target (or more accurately the one that is connected on the LFS, i.e. the lower target here), if the secondary separatrix was far away, is now guided to a secondary SP (solid red arrows). Even without simulations it is expected that the ratio P_{SPp}/P_{SPs} of the fluxes integrated over the areas around the primary and secondary SPs can be tuned by varying the radial position ρ_{x2} of x_2. Qualitatively, this power redirection effect was also expected by Ryutov [18].

Besides this bifurcating effect, the presence of a secondary X-point in the SOL also causes a significant increase in connection length as shown in Fig. 3. While the connection length $L_{c,inner}$ from the outboard mid-plane to the inner target is strongly increased for the DN (dashed blue line) in the near-SOL with respect to that of the SN (dashed green line) the effect on the connection length $L_{c,outer}$ from the outboard mid-plane to the outer target is rather low (cf. blue and green solid lines). For the LFS SF$^-$, however, $L_{c,outer}$ is significantly increased so that $L_{c,inner}$ and $L_{c,outer}$ are approximately equal in the inner SOL region. Assuming that the tendency of a divertor leg to detach depends strongly on L_c, detachment in a LFS SF$^-$ might set in more symmetrically for the two targets.

4. Construction of a computational grid for EMC3-Eirene

The main motivation for applying the 3D code EMC3-Eirene to the toroidally symmetric SF was that it does not necessarily require computational grids aligned to the magnetic flux surfaces, which gives the code a high flexibility in applications to exotic geometries. For the simulations of the SF$^+$ equilibria presented in Ref. [1] we created grids, where the radial surfaces of the confinement- and SOL regions were aligned with the flux surfaces for convenience, while the private flux region covering the structures around the secondary separatrix was a single zone constructed by simple linear interpolation between the separatrix and the wall.

Our initial approach to addressing the SF$^-$ was to apply the same technique for the entire plasma edge covering this region with such a non-flux surface aligned grid. However, due to the enormous difference in flux expansion between the X-point and the regions near the target an extremely high global spatial resolution would have been necessary for the grid. In order to run the code more efficiently in terms of memory consumption and computational time, we now constructed flux surface aligned grids for the LFS SF$^-$ with a far more complex topology, as shown in Fig. 4. This grid is divided into five zones: 'confinement region' (C), 'inner SOL' (IS), 'outer SOL' (OS), 'private flux region' (P) and 'remote areas' one (R1) and two (R2). The outermost regions drawn in fainter colors are defined for the neutrals only. The strike points are numbered in

counter clockwise direction from SP 1 to SP 4 as also shown in Fig. 4. All equilibria used for the grid construction were computed by the Spider equilibrium code [23].

5. Simulation results

5.1. ρ_{x2}-scan

With the computational grids for the SF^+ equilibria ($\rho_{x2} < 1.0$) used in Ref. [1] and the newly constructed series of SF^- grids ($\rho_{x2} > 1.0$), we can now compare nine configurations with ρ_{x2} ranging from 0.988 to 1.020. For $\rho_{x2} = 0.988$ the secondary X-point is so far away from the separatrix that we also refer to this configuration as the SN. An input power of $P_{in} = 300$ kW equally distributed between the electrons and ions was assumed in all simulations in which the separatrix density at the outboard mid-plane was $n_{OMP} = 1.5 \cdot 10^{19}$ m^{-3}. This is a typical value for medium density discharges in TCV. In contrast to the simulations discussed in Sec. 5.3 we focus on pure deuterium simulations here. Two sets of radially, poloidally and toroidally constant transport coefficients were used (A) $D_\perp = 0.5$ m^2/s and $\chi_\perp = 1.5$ m^2/s and (B) $D_\perp = \chi_\perp = 0.6$ m^2/s, where set (B) is the one also used in [1]. 2D profiles of the poloidal cross section of several quantities computed by EMC3-Eirene for (A) are shown in Figs. 5 and 6 for the cases $\rho_{x2} = 1.00048$ and $\rho_{x2} = 1.01432$. The close to exact SF case $\rho_{x2} = 1.00048$ shows the same X-point density peaking effect as observed in previous simulations [1] where the exact SF was approached by SF^+ equilibria. For $\rho_{x2} = 1.01432$ this effect is far less pronounced, but there a region of high density extending from SP 2 to the secondary X-point forms.

Due to the density peaking n_{OMP} differs significantly from the average value $\overline{n}_{LCFS}$ on the first surface inside the separatrix. In order to keep the upstream profiles shown in Fig. 7 as similar as possible it was necessary to fix n_{OMP} instead of $\overline{n}_{LCFS}$ as a constant boundary condition for all simulations during the iteration process.

The particle- and power deposition profiles for four selected ρ_{x2} values are plotted in Fig. 8 (a)-(d). In order to exclude the effect of the non-optimized target inclination angle γ mentioned in the introduction, the *parallel* fluxes $\Gamma_{||}$ and $q_{||}$ are plotted instead of the perpendicular ones to the target surfaces, $j_{sat} = -e\Gamma_\perp$ and $q_\perp$, which are normally measured. The parallel power flux $q_{||} = q_{||,plasma} + (E_{ion} + \frac{1}{2}E_{diss})\Gamma_{||}$ includes the ionization energy of atomic deuterium $E_{ion} = 13.6$ eV and half of the molecular dissociation energy $E_{diss} = 4$ eV and is computed from the plasma fluxes $\Gamma_{||} = n_{se}c_s$ and $q_{||,plasma} = (\gamma_e T_e + \gamma_i T_i)\,\Gamma_{||}$, which are a direct output from the Monte Carlo simulation carried out by EMC3. Here, n_{se} is the density at the sheath edge, $c_s = \sqrt{(T_e + T_i)/m_i}$ is the speed of sound, T_e and T_i are the electron- and ion temperatures and $\gamma_i = 2.5$ and $\gamma_e = 4.5$ the heat sheath transmission factors for ions and electrons. (Note that due to the steep gradients in front of the target the quantities in the last grid cell center are not necessarily exactly the same as those at the boundary surface of that cell, i.e. at the sheath edge) $q_{||}$ is also evaluated for a hypothetical target at the upstream position

according to the same formulae in Fig. 7 (bottom) assuming that the density in front of this target is 1/2 of the unperturbed value. The position ρ_q of the flux surface located at a distance of λ_q at the outboard mid-plane, where $q_{||}$ has fallen to $1/e$ of the value at the separatrix, is also indicated by a blue vertical line in the figure for the two cases. Note that the actual power fluxes without this hypothetical target are different.

Since the radial coordinate ρ is used on the horizontal axis of Fig. 8, the profiles of all four SP can be shown in the same plot. For $\rho_{x2} \lesssim 1$ and $\rho_{x2} \gtrsim 1$ (Fig. 8 (a) and (b)) practically the entire power flux hits SP 1 and 4. Although no dramatic change in the heat flux is observed, note that the topological role of SP 4 changes from a primary to a secondary SP.

Due to the lack of drifts in the simulation $q_{||,max,SP1}$ is significantly larger than $q_{||,max,SP4}$ in contrast to the experimental finding for forward field discharges, as discussed in the introduction. Knowing, however, that the *outer* target is the limiting factor in present day tokamaks, we ignore this fact here and focus only on the effect of ρ_{x2} on SP 2 and SP 4: As expected from geometrical considerations (Sec. 3) an increasing fraction of the power is redirected from SP 4 (red curves) to SP 2 (blue curve) as ρ_{x2} increases (cf. Fig. 8 (b)-(d)). This means that the ratio of power fluxes to SP 2 and SP 4 can be controlled via the radial position of the secondary X-point, which is also seen in Fig. 9, where the the maximum parallel heat flux $q_{||,max}$ (top) and the integral fluxes $I_{SPi} = \int_{SPi} j_{sat} dA$ (middle) and $P_{SPi} = \int_{SPi} q_{\perp} dA$ (bottom) are shown. The data in the bottom plot is normalized to the input power P_{in}. In addition to this power fraction due to direct deposition the plot also shows the fraction of the power transferred to the neutral gas via charge exchange and elastic collisions (label 'gas') as well as that leaving the computational domain through the outer radial grid boundary ('loss'), which add up to 100 % in these simulations in pure deuterium. With the input parameters mentioned above we find an optimum ρ_{x2} defined by $r_{2/4} \equiv q_{||,max,SP4}/q_{||,max,SP2} = 1$ at $\rho_{x2} = 1.013$ for (A) and $\rho_{x2} = 1.010$ for (B), which corresponds to a fraction of the power fall-off length λ_q at the outboard mid-plane (cf. $\rho_q = 1.021$ and $\rho_q = 1.016$ shown in Fig. 7 for (A) and (B), respectively). The maximum heat flux density $q_{||,max,SP4}$ for SP 4 is about two times smaller than the one in a SN like configuration ($\rho_{x2} = 0.9882$) as seen in this Fig. 8 for pure deuterium. If the maximum heat flux density to the outer divertor is actually limiting the maximum extractable power, then the tolerable P_{sep}/R value, commonly regarded as a figure of merit [24, 4, 25], would be twice as high in a LFS SF$^-$compared to a SN. Presumably the increased L_c will cause a detachment of the *outer* target at lower line integrated densities leading to a further reduction of $q_{||,max}$ and therefore an even larger increase of P_{sep}/R.

The expectation that SP 3 receives very little heat is also confirmed by the figure. So if the transport in a reactor in LFS SF$^-$ configuration is not substantially different from that in TCV, a reactor would need to be equipped with three power handling targets.

5.2. ϑ_{x2}-scan

Apart from studying the effect of the *radial* position of the secondary X-point ρ_{x2} on the power deposition profiles the effect of its *poloidal* position ϑ_{x2} was also investigated. For this purpose the radial magnetic position of x_2 was kept constant at $\rho_{x2} \sim 1.014$ while changing ϑ_{x2} from 0.91 to 1.18 which corresponds to a spatial distance of roughly 12 cm. For comparison the minor radius of the plasma is $a = 22$ cm. As shown in Fig. 10 the fluxes, in particular the integral ones, depend rather little on ϑ_{x2} as expected from the geometrical considerations of Secs. 2 and 3.

5.3. Impurity transport simulations

A fusion reactor will need to be operated at very high radiative fractions of the order of 95 % of the power produced and absorbed in the confinement region. In addition to the findings in a pure deuterium simulation the dependence of the impurity particle- and radiation distribution on ρ_{x2} is, therefore, also of high importance, when designing such a device. In order to address this question we performed EMC3 impurity transport simulations with nitrogen and neon, for which the atomic data was taken from the ADAS data base [26] (format: ADF11, dataset: 1996). EMC3 solves the force balance equation for the impurities, while it neglects their contribution in the main ion species continuity- and momentum equations. Their radiated power on the other hand is taken into account self-consistently in the energy equation during the iteration process. Given that the number of iterations required to reach acceptable levels of convergence increases strongly with increasing impurity radiation $P_{rad,imp}$, we limit our analysis to $P_{rad,imp}/P_{in} = 20$ % here. The impurity influx density Γ_Z is assumed to be linear with that of deuterium Γ_D to the target surfaces. This is described formally by a constant sputtering yield $Y = -\Gamma_Z/\Gamma_D$ which is chosen such that the assumed radiation level is achieved. A more realistic impurity source model is foreseen to be implemented for the near future. 2D profiles of the total impurity density $\sum_Z n_Z$ and the radiation density S_Z are shown in Figs. 12 and 13 for nitrogen and neon, respectively. While practically all impurities accumulate and radiate very close to the targets for $\rho_{x2} = 0.98824$, they penetrate deeper into the SOL plasma for higher ρ_{x2} values. For configurations close to the exact SF a maximum in impurity radiation is found around the X-point, part of it inside the confinement region. With further increasing ρ_{x2} the radiation inside the separatrix is decreasing again and a radiation cloud is forming between the two X-points for $\rho_{x2} = 1.00308$. Such a radiation cloud converts heat into isotropically emitted radiation further upstream and could help to reduce the peak power load on the targets. Given that the radiation cloud is located at the LFS of the primary X-point in a LFS SF^- we can expect that the targets connected on the LFS (SP 2 and SP 4) are more affected by this effect than that on the HFS.

This is in fact observed when comparing the target $q_{||,max}$ profiles in pure deuterium (Fig. 9, top) to those with nitrogen and neon impurities (Fig. 11, top). While the optimum ρ_{x2} position was $\rho_{x2} = 1.013$ for the pure deuterium case it is slightly shifted outwards

to $\rho_{x2} = 1.016$ for the case with nitrogen impurities. By introducing nitrogen the maximum parallel power flux density to the inner target is reduced to $q_{||,max,SP1} = 12.2$ MW/m^2, i.e. 42 % less than the value for pure deuterium $q_{||,max,SP1} = 17.3$ MW/m^2 in the respective optimum case. The targets connected via the LFS SOL (SP 2 and SP 4) experience a significantly larger reduction of 71 % comparing the case with ($q_{||,max,SP2} = q_{||,max,SP4} = 2.9$ MW/m^2) and without nitrogen ($q_{||,max,SP2} = q_{||,max,SP4} = 5.0$ MW/m^2). In addition to the power flux reduction due to geometry described in Sec. 5.1 the asymmetric impurity radiation effect motivates the expectation that a well tuned LFS SF$^-$ achieves much more symmetric power deposition profiles compared to a SN in the experiment (and in simulations where drifts are included). This is another reason to expect an increase of the maximum tolerable P_{sep}/R for a LFS SF$^-$.

6. Currents in the poloidal field coils

It is well known that high-order multipole fields have a short decay length. For this reason one can expect that significantly larger currents are required in the poloidal field (PF) coils and/or a shorter distance between these coils and the main plasma to produce an exact SF compared to a SN. The proximity of the coils to the fusion plasma and the high currents are both challenging in a reactor. The first because of the required screening of the superconductors against the fusion neutrons and the latter because of the limited current densities in a superconductor and the large forces acting among the coils. Lackner and Zohm [27] therefore came to the conclusion that an exact SF with the X-point at the same position as that of the SN would not be realizable in ASDEX Upgrade. Assuming that the superconducting PF coils are operated at the maximum tolerable current density (i.e. slightly below the critical current density, where the conductor looses its superconductivity) the cross section of the coil is proportional to the required product of the current I_{PF} and the number of turns N_{PF} of the super conductor in the coil. The volume of the coil and therefore the amount of superconducting material and its price are proportional to the product of the cross section and the major radius R_{PF} of the coil. Therefore a 'cost parameter' can be defined as

$$p_{cost} = \sum_i |I_{PF_i}| \, N_{PF_i} R_{PF_i} \ , \tag{1}$$

where the sum extends over all PF coils.

For TCV this parameter is evaluated for selected configurations in Tab. 2. As expected p_{cost} is increasing from 0.74 MAt m to 1.25 MAt m when passing from the SN to the exact SF (lines 1–4). So similar to the result from AUG the exact SF configuration is significantly more 'expensive' compared to the SN. In Sec. 5.1 we have seen, however, that the exact SF does not provide the optimum power repartition in TCV but rather a SF with $\rho_{x2} = 1.017$. A configuration close to this value is significantly 'cheaper' as shown by line 5 in Tab. 2. Additionally, we have seen in Sec. 5.2 that ϑ_{x2} can be varied, while keeping the ratio of power flux densities close to $r_{2/4} = 1$. As shown by the following line 6 a configuration with the same ρ_{x2} but larger ϑ_{x2} is almost as 'cheap'

as the SN, i.e. $p_{cost} = 0.78$ MAt m.
How do these results now extrapolate to a reactor, i.e. to a machine with a larger major radius? Given that the power fall-off length is expected to be of the same order as AUG and JET and not to scale with machine size [28] the optimum ρ_{x2} is expected to be much closer to unity. The last line of Tab. 2 shows, however, that a 'cheap' configuration can be found with $\rho_{x2} \sim 1.0$ and $\vartheta_{x2} = 1.38$, i.e. with a certain spatial separation σ of the X-points.
One should note that this last configuration has a rather large divertor volume, which might complicate the maximization of the volume of the confinement region – a very important optimization criterion for a reactor. Furthermore, the PF coils are located inside the toroidal field (TF) coils in TCV, which is likely not feasible in a reactor. So we still expect that a reactor designed with a SF divertor will be more expensive than one designed as a SN. However, the findings described in this article show that it is worthwhile to take such a configuration into consideration. The final answer concerning the feasibility of a SF configuration a reactor should be given by magnetic equilibrium calculations allowing the optimization of the spatial locations of the coils.

7. Summary and outlook

We reported on EMC3-Eirene simulations of TCV snowflake minus equilibria, where the secondary X-point (x_2) is located in the common flux region of the primary separatrix on the low-field side (LFS SF^-), and compared these to earlier simulations with x_2 in the private flux region (SF^+) presented in Ref. [1]. Nine configurations covering a range $\rho_{x2} = 0.988 \ldots 1.020$ of the radial magnetic positions of x_2 were analyzed. The simulations were carried out for pure deuterium with two different sets of diffusive transport coefficients and with nitrogen- and neon impurities radiating a fixed amount of 20 % of the input power.
While in the SF^+ the power redirection to the secondary strike points (SP) was of the order of 1 % according to simulations with a spatially constant diffusivity and 10 % experimentally only [1], a much higher power redirection accompanied by a reduction of the peak heat flux density to the outer target of up to a factor of two was found for the LFS SF^- configurations in pure deuterium without drifts. The figure of merit for acceptable power flux P_{sep}/R is thus expected to increase for such a configuration. The power mitigation mechanism is similar to that of the topologically identical double null (DN) configuration, where part of the power flux to the *inner,* moderately loaded target is redirected to the upper one. In the LFS SF^- on the other hand this redirection affects the *outer,* otherwise heavily loaded target. As expected from geometrical considerations ρ_{x2} can be used to tune the ratio $r_{2/4} = q_{||,max,SP2}/q_{||,max,SP4}$ of maximum parallel power flux densities to SP 2 and SP 4 as well as that of the spatially integrated power fluxes. The optimum $r_{2/4} = 1$ is found for $\rho_{x2} = 1.013$, which corresponds to a fraction of the power fall-off length λ_q at the outboard mid-plane located on the $\rho_q = 1.021$ flux surface.

In these simulations the inner SP 1 receives the largest power flux density in contrast to the experimental observation, which is attributed to the lack of drifts in the code. The implementation of these terms is foreseen for the long term future.
The impurity radiation in the simulations of discharges with nitrogen and neon impurities was observed to reduce the power fluxes to the targets significantly. Due to an accumulation effect of the impurities between the strike- and X-points a particularly strong reduction of the peak power flux density is observed for the outer SPs as well as a shift of the optimum to $\rho_{x2} = 1.016$. The simulations are based on a strongly simplified impurity source model described by a constant sputtering yield. A more refined impurity source model is foreseen to be implemented in the future.
Assuming that the tendency of a divertor leg to detach depends strongly on the (outboard mid-plane to target) connection length, the outer targets in a LFS SF^- are expected to detach at lower line-integrated densities compared to a single null configuration, which would enable an even higher increase in the figure of merit P_{sep}/R.
An important result was also that the power repartition does not depend strongly on the poloidal position ϑ_{x2} of the secondary X-point. ϑ_{x2} can probably be chosen such that the engineering limits on $\theta_\perp$ can be met at the target, while keeping the divertor closure high, and the cost parameter defined in Sec. 6 low. In this sense these results lead to more optimistic conclusions concerning the benefits of a snowflake as well as its realizability in a reactor than the ones drawn in previous works [1, 27].

8. Acknowledgements

This work has been carried out within the framework of the EUROfusion Consortium and has received funding from the Euratom research and training programme 2014-2018 under grant agreement No 633053. The views and opinions expressed herein do not necessarily reflect those of the European Commission. We would like to thank Alberto Loarte, Christopher Lowry, Richard Pitts and Felix Reimold for the fruitful discussions on the divertor optimization.

9. References

[1] Lunt T. *et al.* 2014 *Plasma Phys. Control. Fusion* **56** 035009
[2] Reimerdes H. *et al.* 2013 *Plasma Phys. Contr. Fusion* **55** 124027
[3] Reimold F. *et al.* 2014 *J. Nucl. Mater.* (published online, reference not available yet)
[4] Zohm H. *et al.* 2013 *Nucl. Fusion* **53** 073019
[5] Lackner K. *et al.* 1994 *Plasma Phys. Contr. Fusion* **36** B79–B92
[6] Wagner F. 2007 *Plasma Phys. Contr. Fusion* **49** B1–B33
[7] Aho-Mantila L. *et al.* 2012 *Nucl. Fusion* **52** 103006
[8] Loarte A. *el al.* 2001 *Plasma Phys. Contr. Fusion* **43** R183–R224
[9] Eich T. *et al.* 2007 *Plasma Phys. Control. Fusion* **49** 573–604
[10] Loarte A. *et al.* 1998 *Nucl. Fusion* **38** 331–371
[11] Potzel S. *et al.* 2014 *Nucl. Fusion* **54** 013001
[12] Wenninger R. *et al.* 2015 to be submitted to *Nucl. Fusion*
[13] Kotschenreuther M. *et al.* 2007 *Phys. of Plasmas* **14** 072502

[14] Horton L. *et al.* 1999 *Nucl. Fusion* **39** 1
[15] Shimomura Y. *et al.* 1983 *Nucl. Fusion* **23** 869–879
[16] Ryutov D.D. *et al.* 2007 *Phys. of Plasmas* **14** 064502
[17] Ryutov D.D. *et al.* 2012 *Plasma Phys. Contr. Fusion* **54** 124050
[18] Ryutov D.D. *et al.* 2010 *Plasma Phys. Contr. Fusion* **52** 105001
[19] Ryutov D.D. *et al.* 2012 *Proceedings of the 24th IAEA Fusion Energy Conference, San Diego, USA, 8-13 October 2012* TH/P4-18
[20] Canal G. *et al.* 2015 *to be submitted to Nucl. Fusion*
[21] Reiter D. *et al.* 2005 *Fus. Sci. Tec.* **47** 172–186
[22] Feng Y. *et al.* 2004 *Contrib. Plasma Phys.* **44**, No. 1–3, 57–69
[23] Ivanov A.A. *et al.* 2009 **39** *The SPIDER Code - Solution of Direct and Inverse Problems for Free Boundary Tokamak Plasma Equilibrium* Keldysh Institute preprints
[24] Kallenbach A. *et al.* 2013 *Plasma Phys. Control. Fusion* **55** 124041
[25] Lackner K. *et al.* 1994 *Comments Plasma Phys. Contr. Fusion* **15** 359
[26] Summers H.P., 1994 *Atomic data and analysis structure users manual* JET-IR 06 (Abingdon: JET Joint Undertaking).
[27] Lackner K., Zohm H. 2013 *Fus. Sci. and Tec.* **63** No. 1, 43–48
[28] Eich T. *et al.* 2011 *Phys. Rev. Lett.* **107** 215001

Radial position	Poloidal position	Name	Abbreviation
$\rho_{x2} = 1$	$\vartheta_{x2} \sim 0$	connected double null	(c)DN
$\rho_{x2} > 1$	$\vartheta_{x2} \sim 0$	disconnected double null	(d)DN
$\rho_{x2} = 1$	$\vartheta_{x2} \pm 1$	exact snowflake	SF
$\rho_{x2} > 1$	$\vartheta_{x2} \sim +1$	snowflake minus LFS	SF^- LFS
$\rho_{x2} > 1$	$\vartheta_{x2} \sim -1$	snowflake minus HFS	SF^- HFS
$\rho_{x2} < 1$	$\vartheta_{x2} \sim \pm 1$	snowflake plus	SF^+
$\rho_{x2} \geq 1$	$\vartheta_{x2} = \pm 2$	X-point divertor	XPD
$\rho_{x2} \geq 1$	$\lvert\vartheta_{x2}\rvert > 2$	X-divertor	XD
$\rho_{x2} \gg 1$ or $\rho_{x2} \ll 1$	any	single-null	SN

Table 1. Denomination of different configurations with two X-points according to the ρ_{x2} and ϑ_{x2} locations of the secondary X-point.

#	σ	θ [deg]	ρ_{x2}	ϑ_{x2}	I_{PFmax} [MA]	p_{cost} [MAt m]	Comment
1	1.00	90	0.9882	1.026	4.16	0.74	SN
2	0.50	90	0.9971	1.065	3.92	0.87	
3	0.10	90	1.0000	1.006	5.10	1.15	
4	0.01	90	1.0000	1.000	5.96	1.25	close to exact SF
5	0.80	10	1.0143	0.962	5.85	1.07	optimum LFS SF^- TCV
6	1.15	35	1.0145	1.179	4.90	0.78	
7	1.00	55	1.0011	1.384	4.57	0.75	expected optimum in reactor

Table 2. Comparison of the maximum PF coil current I_{PFmax} and the cost parameter p_{cost} defined by Eq. 1 for selected configurations with two X-points in TCV characterized by the geometrical parameters σ and θ or the magnetic ones ρ_{x2} and ϑ_{x2}.

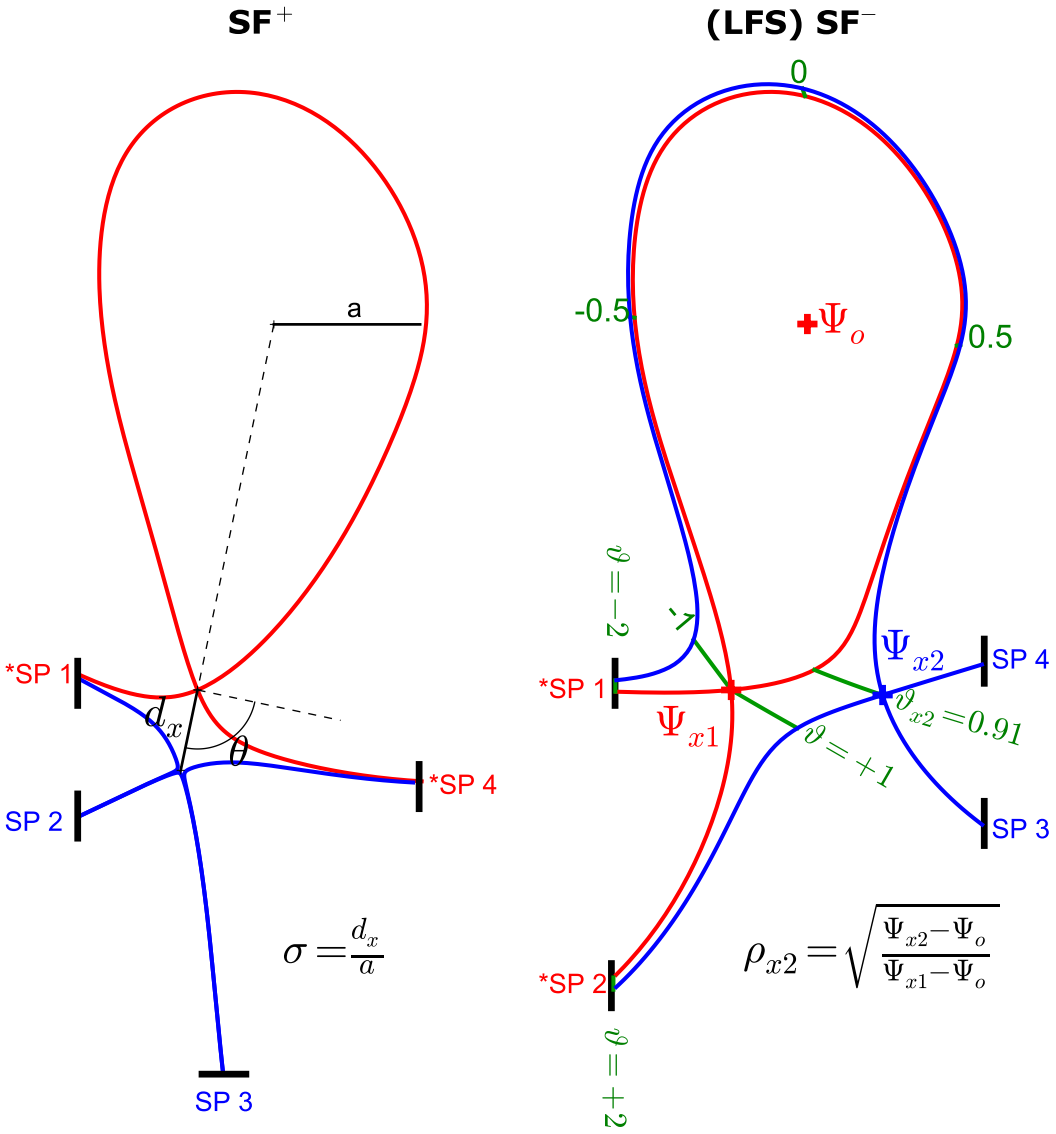

Figure 1. Geometry of the SF^+ (left) and (LFS) SF^- (right) configurations. On the left the definition of the geometrical coordinates (σ, θ) is illustrated while the newly introduced magnetic coordinates $(\rho_{x2}, \vartheta_{x2})$ are illustrated on the right. Note that both parameter sets are defined for both configurations.

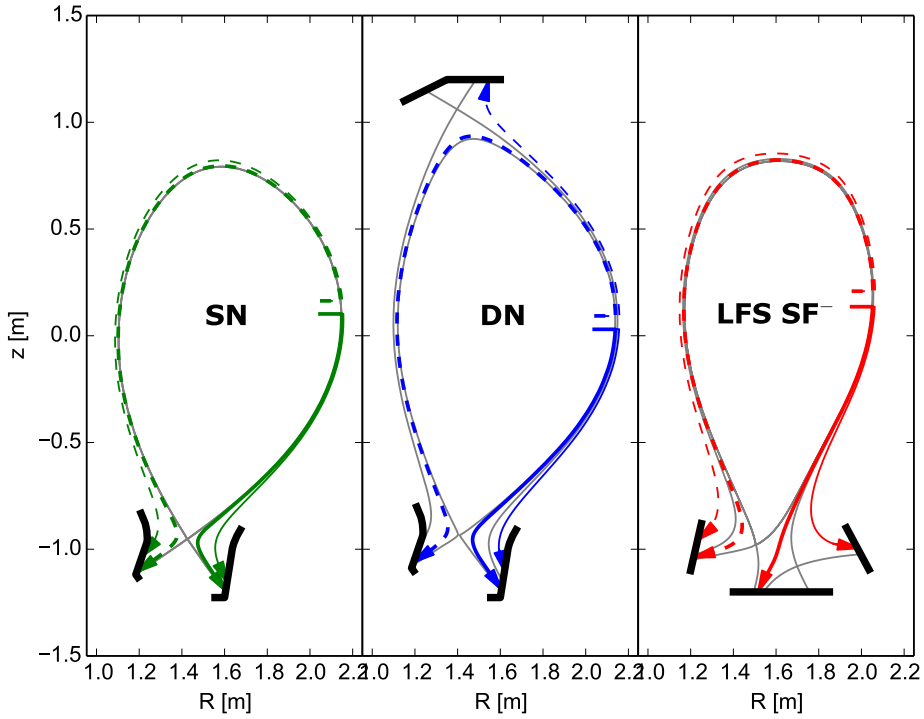

Figure 2. Illustration of the dominant power fluxes in single-null (SN), double-null (DN) and LFS snowflake minus (LFS SF^-) configurations based on AUG equilibria with 800 kA plasma current. Note that the target geometry is not the real one but is compatible with the AUG vacuum vessel geometry.

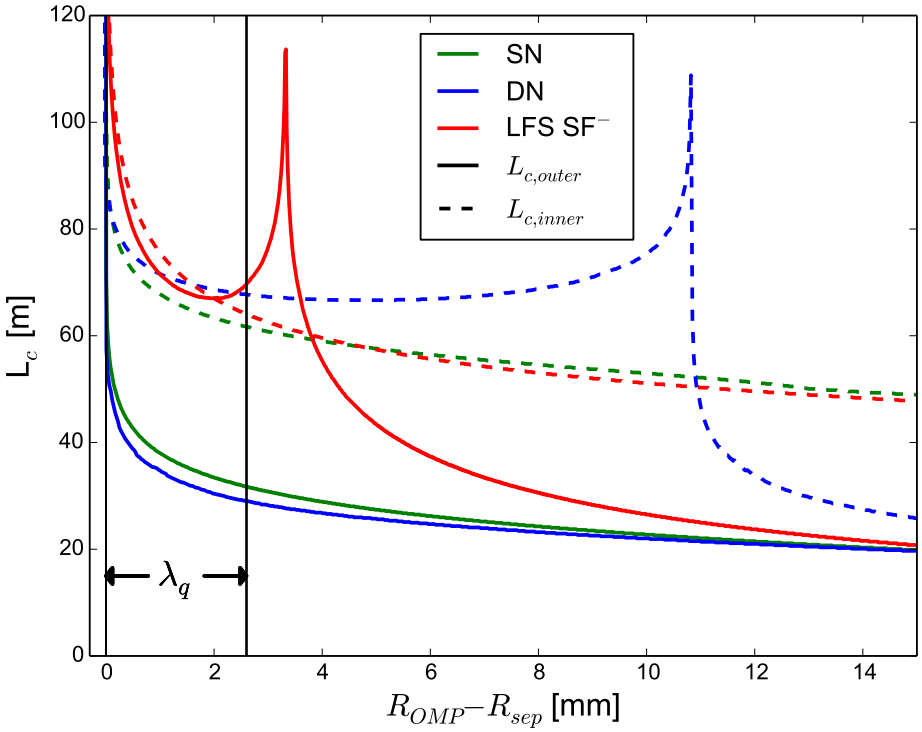

Figure 3. Connection length from the outboard mid-plane to the inner (dashed lines) and outer (solid lines) targets for the single-null (SN, green), double null (DN, blue) and LFS snowflake minus (LFS SF$^-$, red) configuration illustrated in Fig. 2. A typical power fall-off length in AUG is $\lambda_q = 2.6$ mm. The same colors and line styles as in Fig. 2 were used.

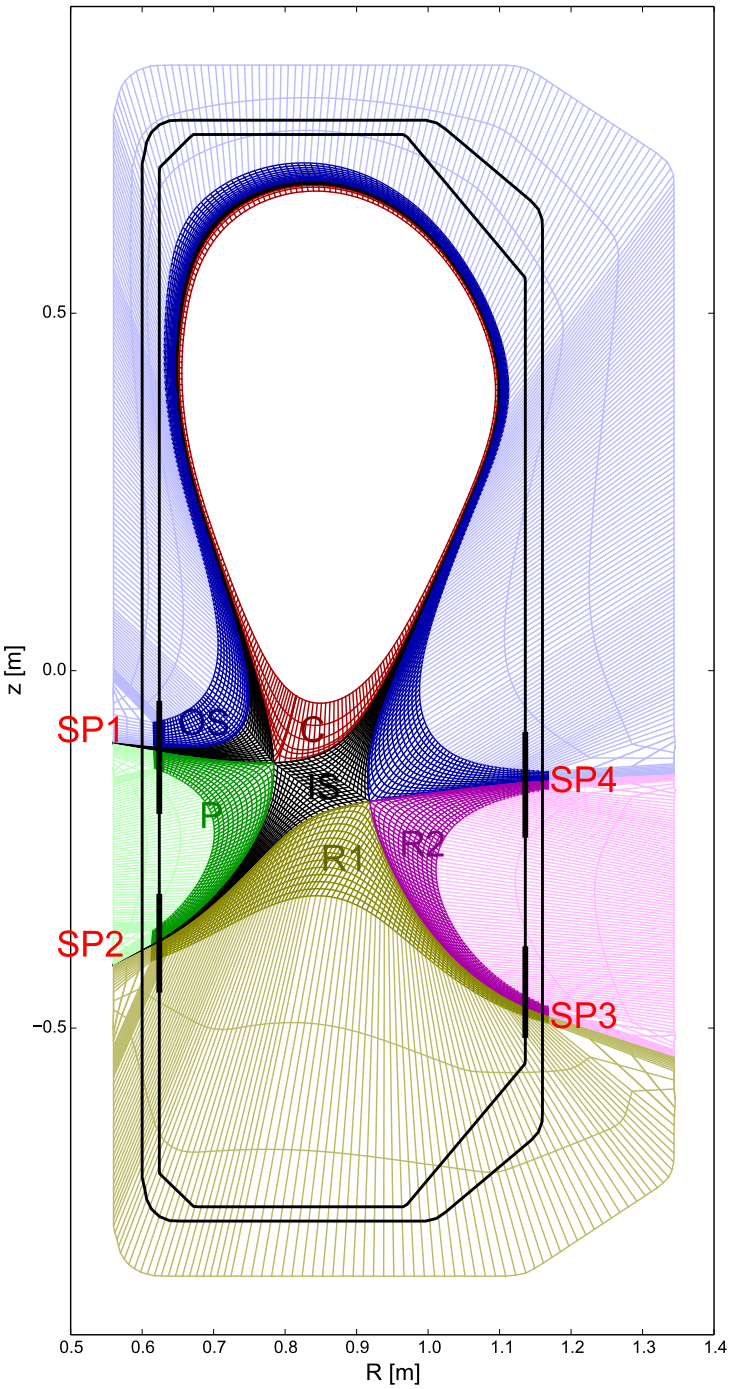

Figure 4. Poloidal projection of the computational grid for a LFS SF$^-$ configuration with $\rho_{x2} = 1.0075$ and $\vartheta_{x2} = 0.96$.

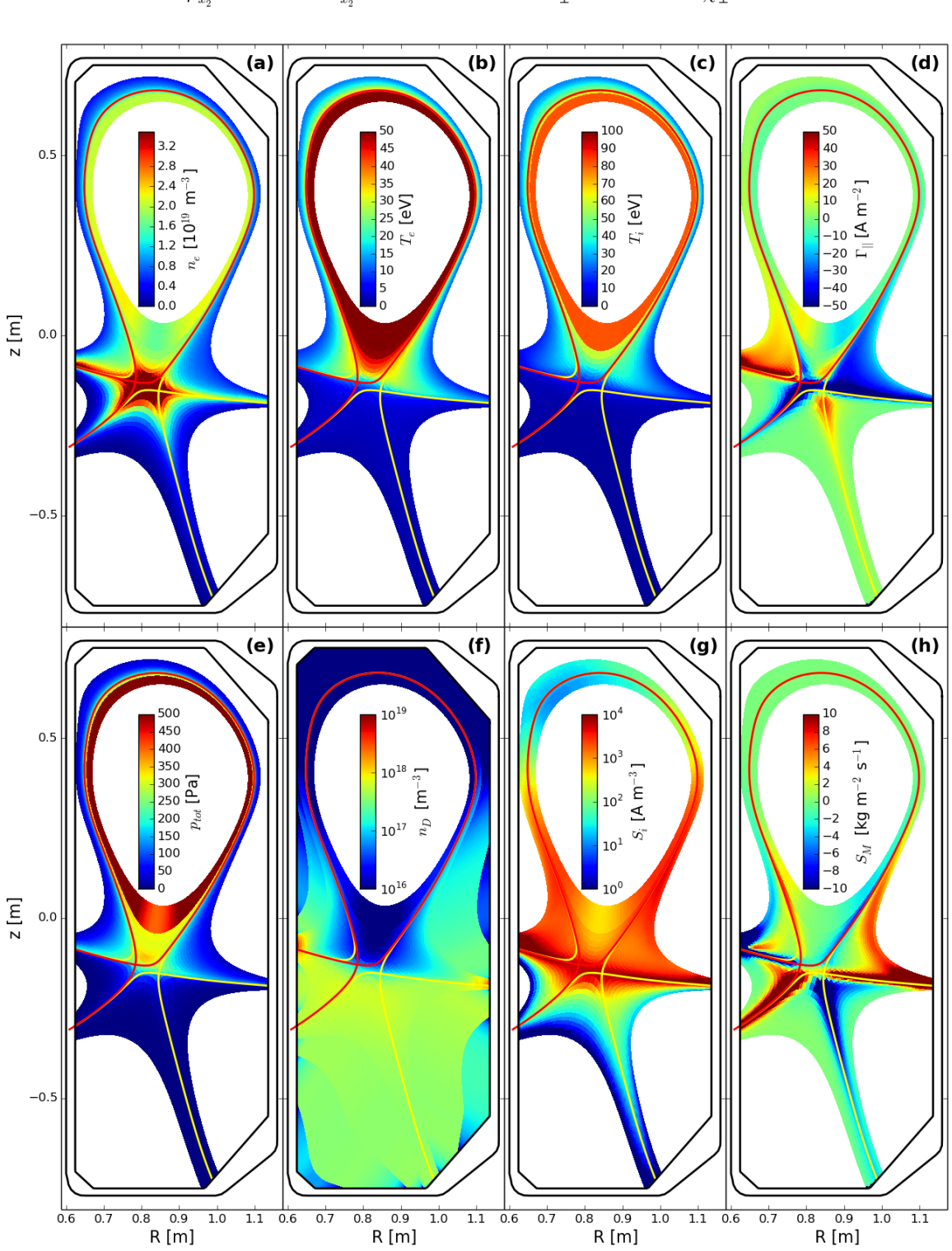

Figure 5. Poloidal cross section of density (a), electron- (b) and ion temperature (c), parallel particle flux (d), total pressure (e), neutral deuterium density (f), ionization strength (g) and momentum source (h) for $\rho_{x2} = 1.00048$ and $\vartheta_{x2} = 0.97$. The density at the outboard mid-plane is $n_{OMP} = 1.5 \cdot 10^{19}$ m^{-3}. The primary separatrix is shown in red and the secondary one in yellow.

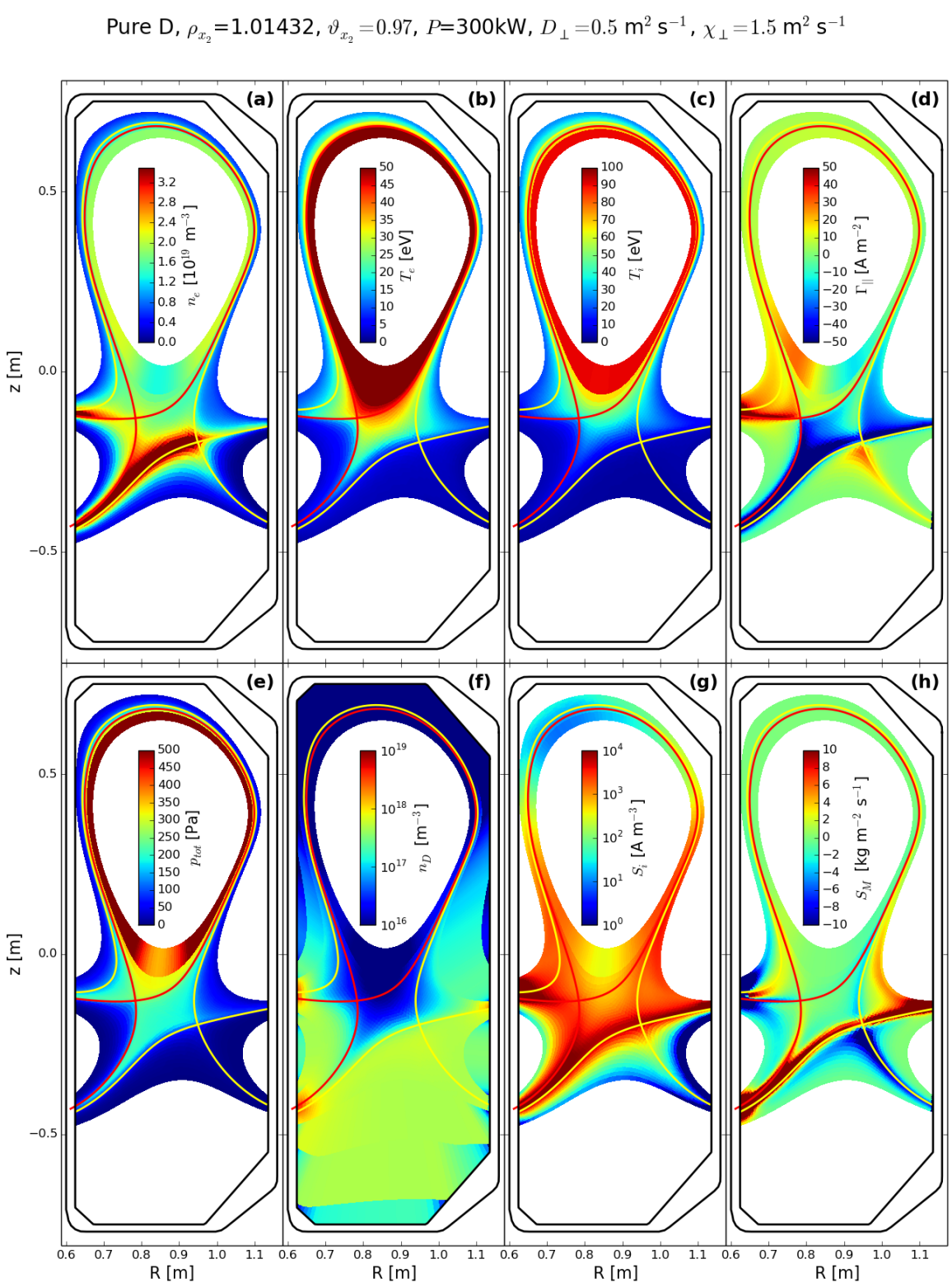

Figure 6. Same as Fig. 5 but for $\rho_{x2} = 1.01432$ and $\vartheta_{x2} = 0.96$.

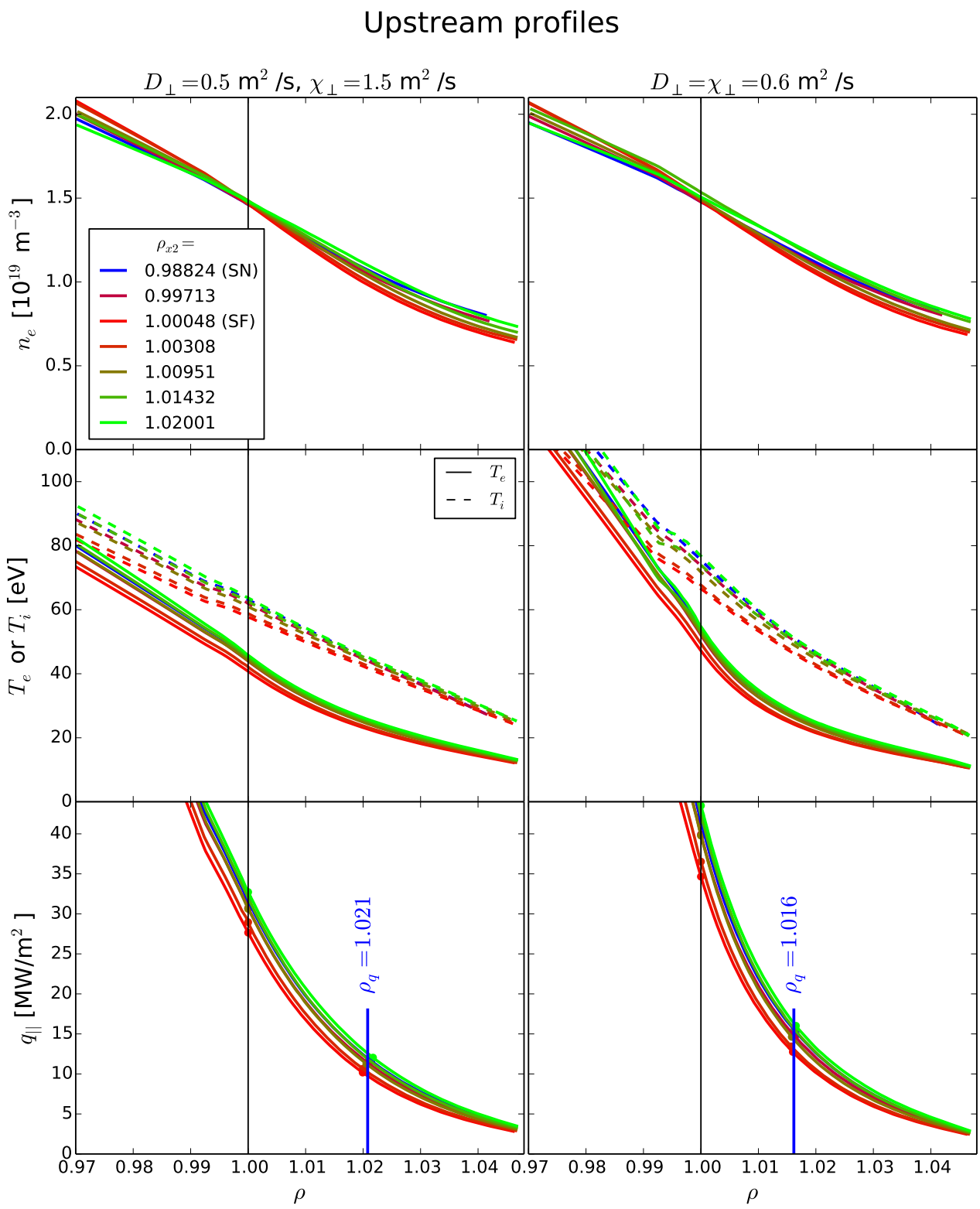

Figure 7. Upstream density (top), temperature (middle) and thermal pressure (bottom) profiles evaluated at the outboard mid-plane.

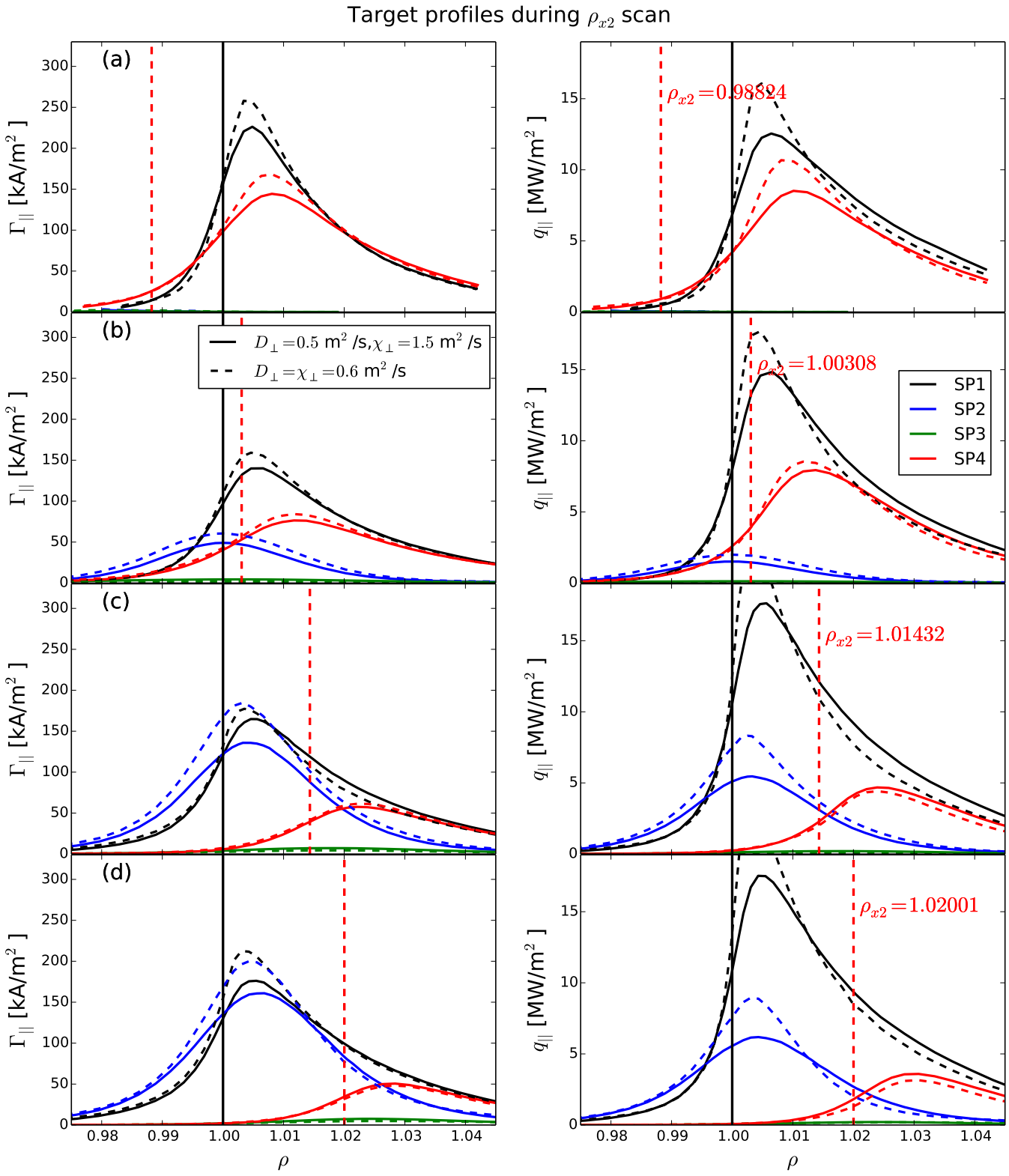

Figure 8. Parallel particle- (left) and power (right) fluxes for the strike points SP 1...SP 4 as a function of the magnetic coordinate $\rho = \sqrt{(\Psi - \Psi_o)/(\Psi_{x1} - \Psi_o)}$. The magnetic position of the secondary X-point is shown by the red dashed vertical line.

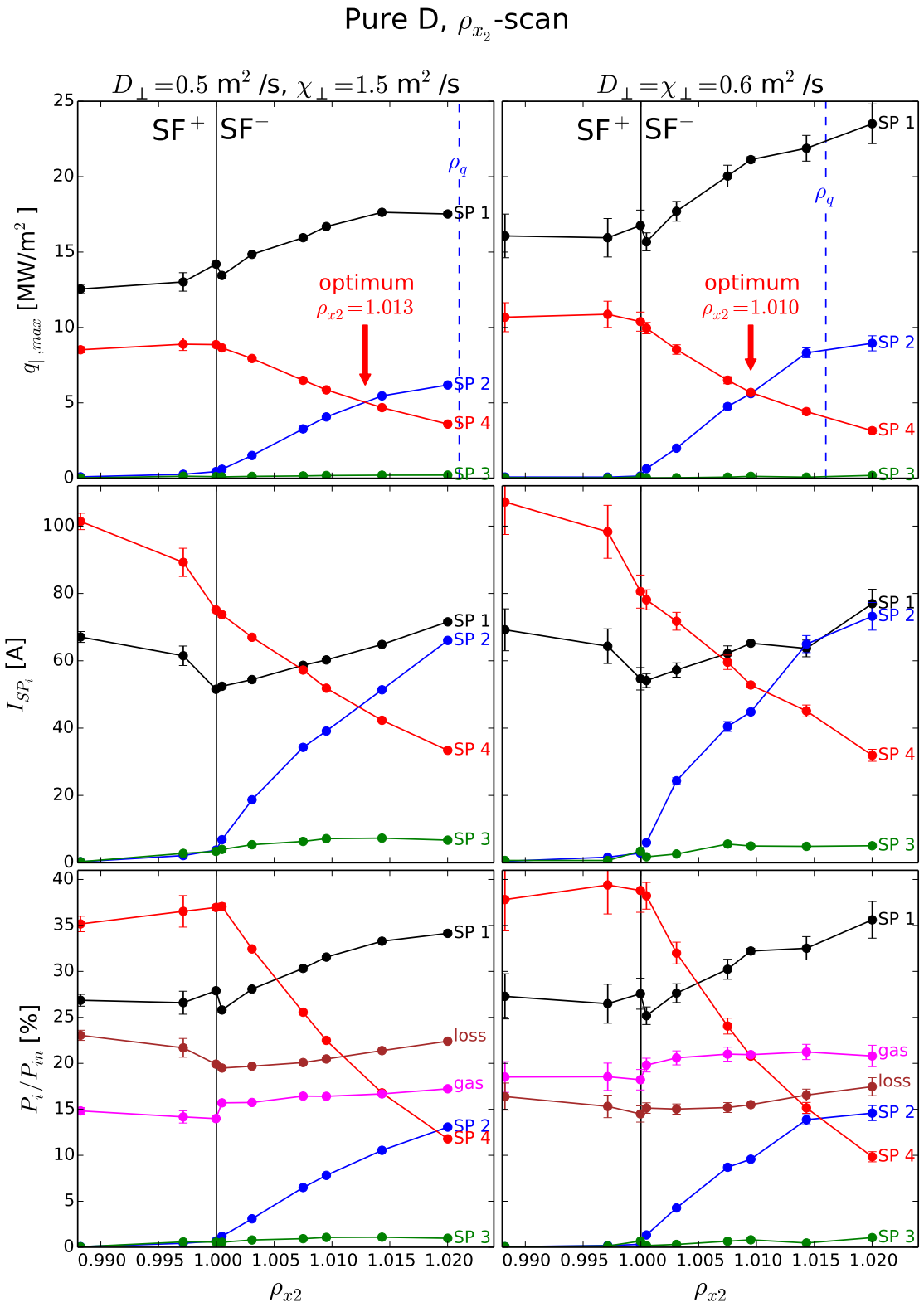

Figure 9. Peak parallel power flux density $q_{||,max}$ (top) and particle- (middle) and power (bottom) fluxes integrated over the areas near the SPs on the target for a series of nine pure deuterium simulations with different radial positions ρ_{x2} of the secondary X-point. Two sets of transport parameters were used, $D_\perp = 0.5$ m^2/s and $\chi_\perp = 1.5$ m^2/s (left) and $D_\perp = \chi_\perp = 0.6$ m^2/s (right).

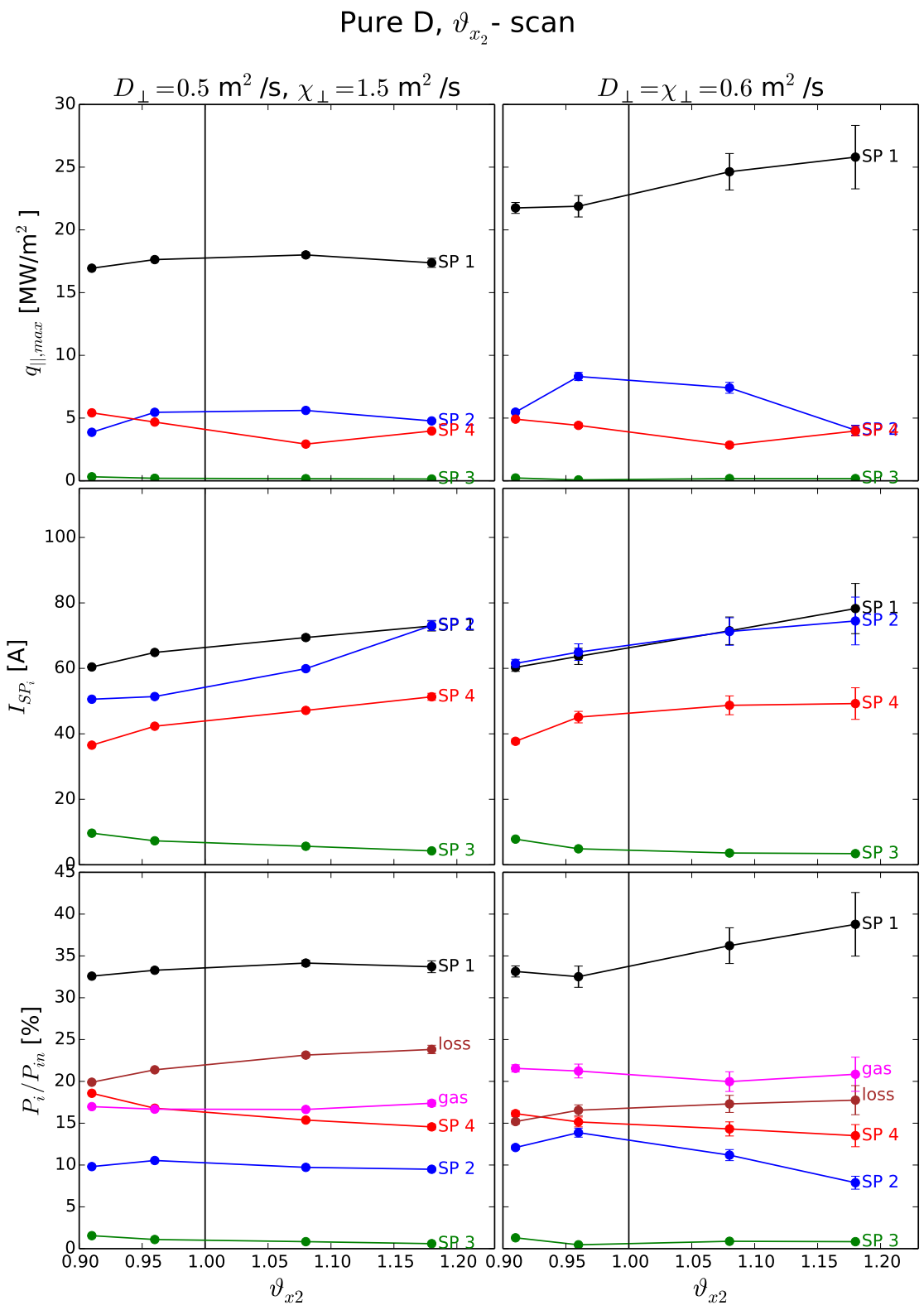

Figure 10. Same quantities as in Fig. 9 but at a fixed $\rho_{x2} = 1.014$ varying the poloidal position ϑ_{x2} of the secondary X-point.

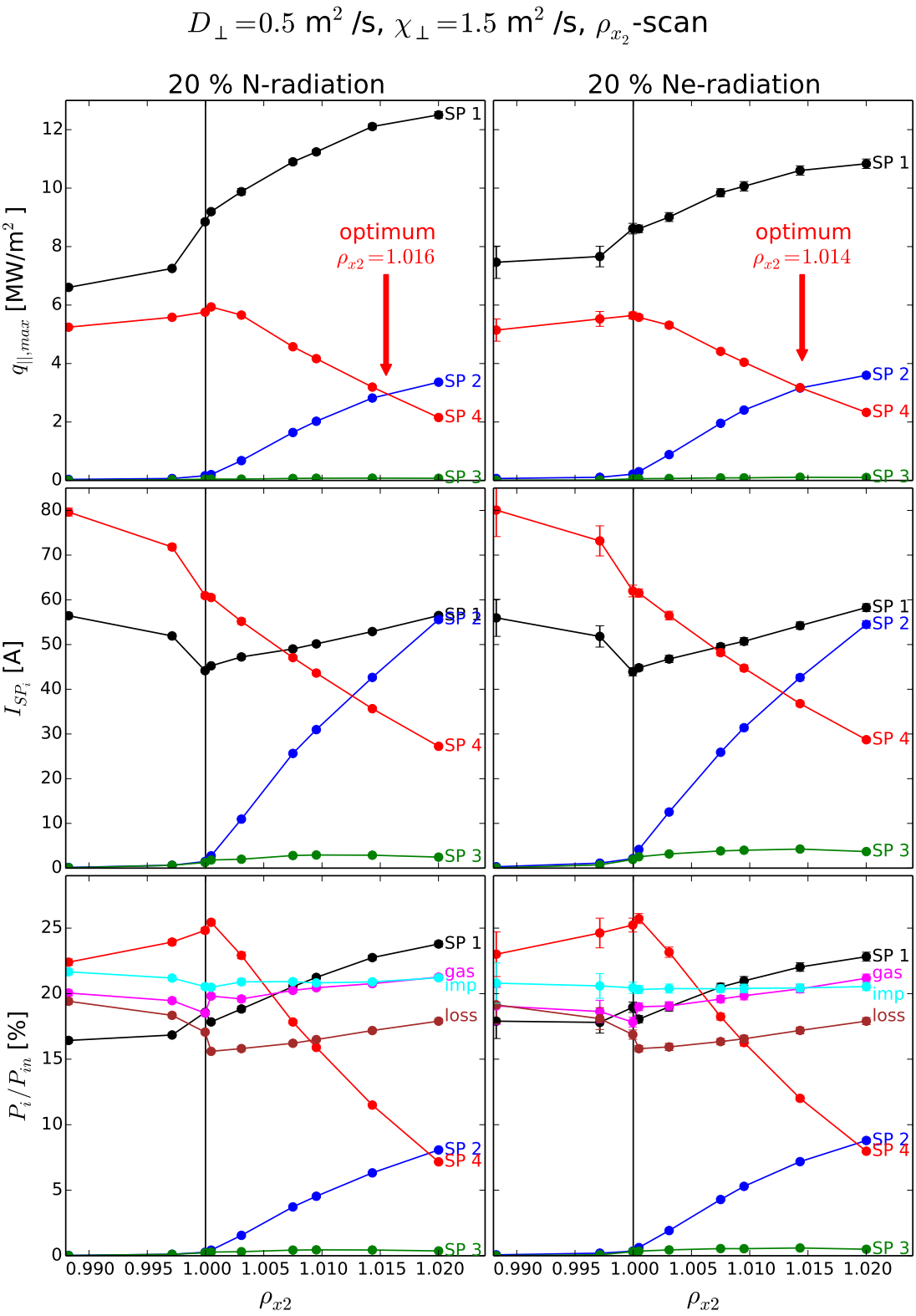

Figure 11. Same as Fig. 9 but for $D_\perp = 0.5$ m^2/s and $\chi_\perp = 1.5$ m^2/s assuming that 20 % of the input power is radiated by impurities. Nitrogen (left) and neon (right) were used as impurity species that are started at the targets according to a strongly simplified impurity source model described by a constant sputtering yield.

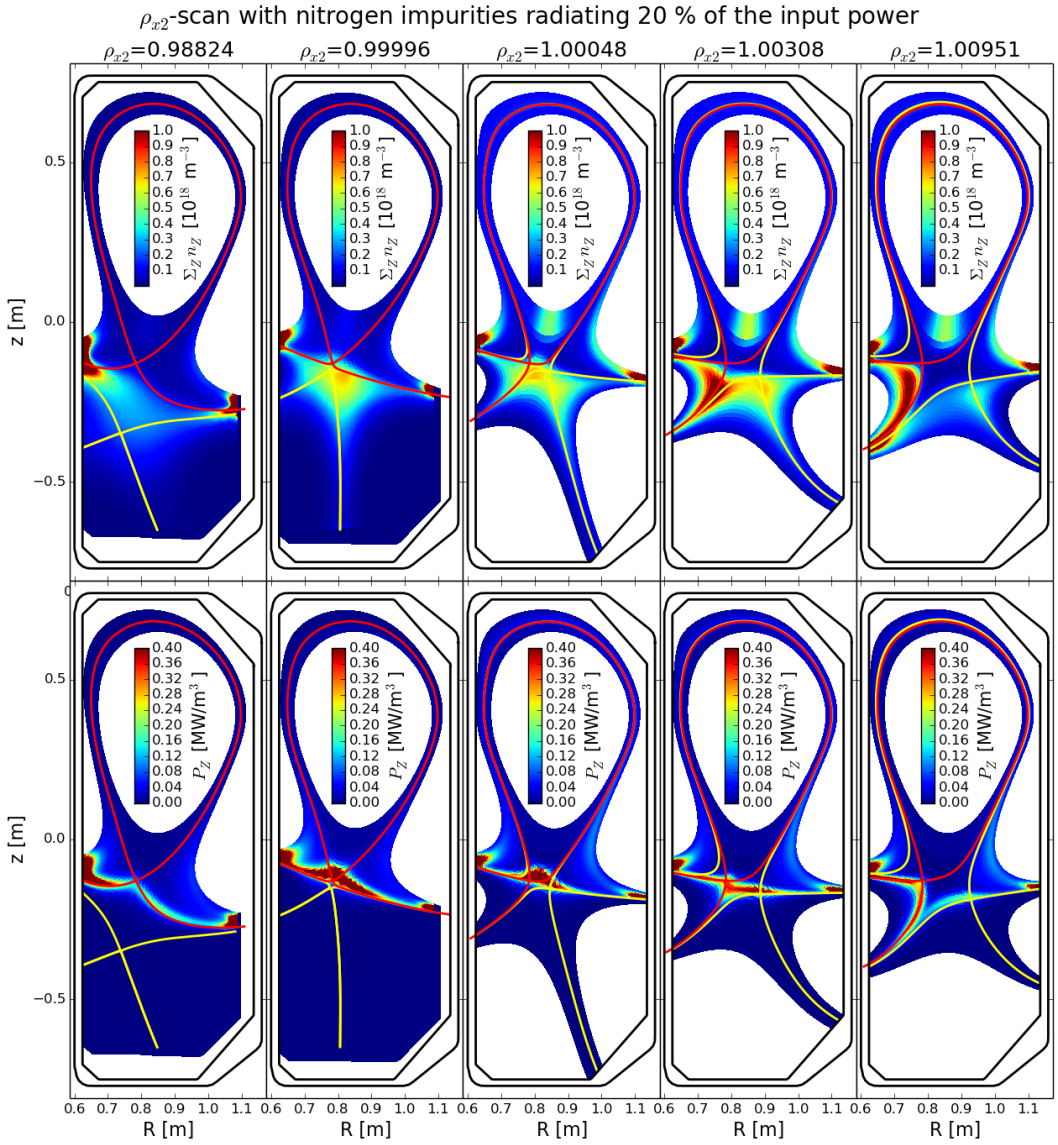

Figure 12. 2D distribution of the total nitrogen density (top) and radiation (bottom) for five configurations with different ρ_{x2} values.

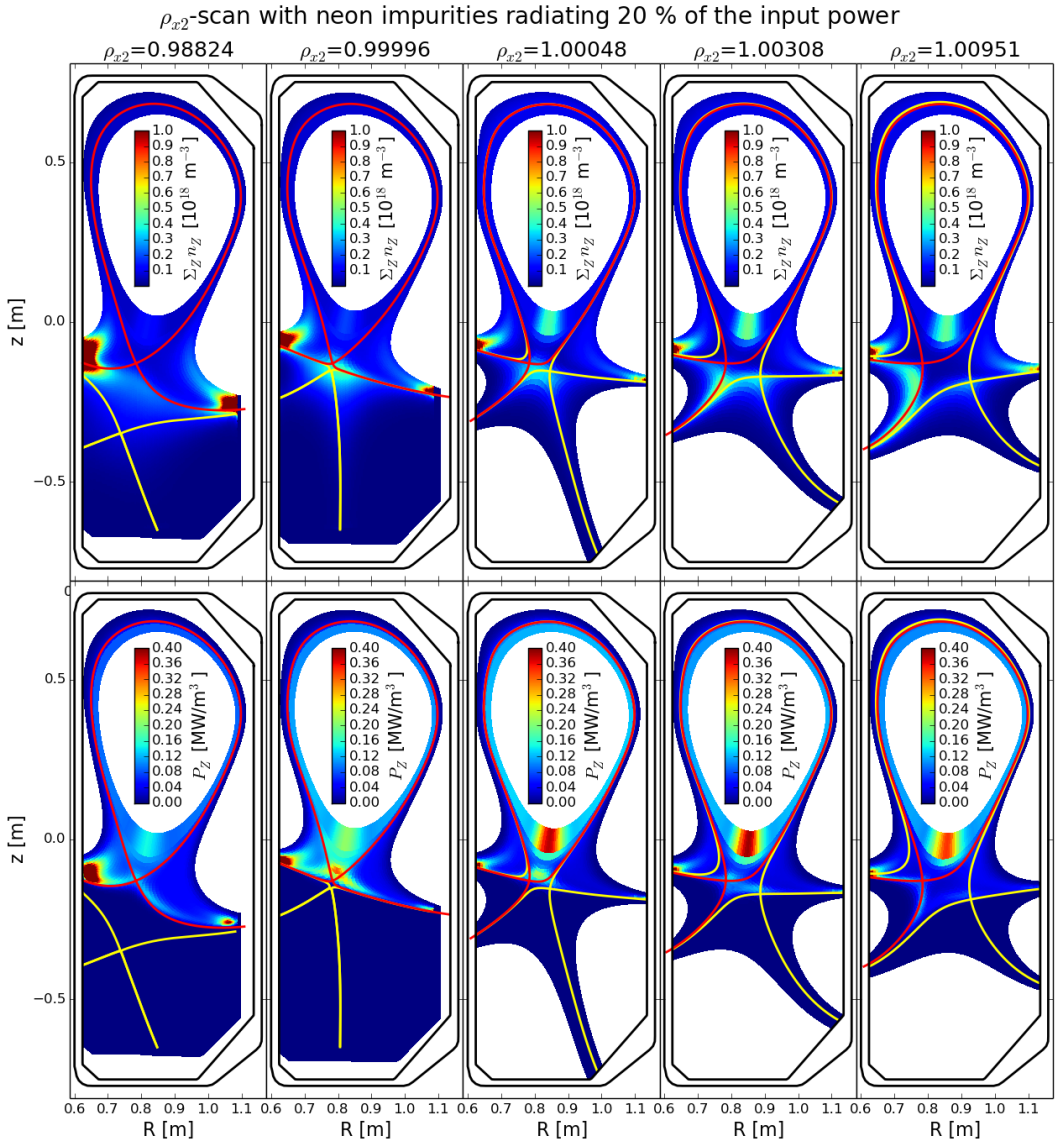

Figure 13. Same as Fig. 12 but for neon

Appendix A. Geometrical limitation of flux expansion and target inclination angle

The magnetic flux expansion at the target is defined as the radial distance dr_t of two neighboring flux surfaces at the target to that at an upstream position (in general the outboard mid-plane) dr_u, which is given by

$$f_{x,mag} \equiv \frac{dr_t}{dr_u} = \frac{R_u B_{\theta,u}}{R_t B_{\theta,t}} \ . \tag{A.1}$$

If no power was lost along the field line, all power that enters the radial upstream interval dr_u will be mapped to that at the target $ds = dr_u f_{x,mag}/\cos(\gamma)$ in the poloidal plane, where γ is the poloidal target tilt angle with respect to the flux surface (cf. Fig. A1 left). Thus increasing the flux expansion (e.g. by decreasing $B_{\theta,t}$) or increasing γ are effective ways of distributing the power over a larger poloidal interval ds on the target. Note that some authors, like those of Ref. [28], define $f_x = f_{x,mag}/\cos(\gamma)$ as flux expansion.
If the target was perfectly symmetric in toroidal direction this would also cause an increase of the area $dA = 2\pi R ds$ onto which this power is distributed and therefore a decrease of the power flux density. From the engineering point of view, however, it seems to be completely unrealistic to build a divertor target from one single piece inside the toroidal field coils (which would need to be assembled around it) with no surface roughness. The divertor targets in many modern tokamaks are composed of tiles that have a finite toroidal width w and a gap with the extension g between them to cope with the thermal expansion (cf. Fig. A1 right). In order to avoid field lines to penetrate the gap between the tiles they are also tilted in *toroidal* direction by an angle α around the axis ζ in the figure.
Decreasing the poloidal field $B_{\theta,t}$ at the target it is unavoidable to decrease also the field line incidence angle at the target given by

$$\theta_\perp = \tan^{-1}\left(B_{\xi,t}/B_{\phi,t}\right) = \tan^{-1}\left(\cos(\gamma)\, B_{\theta,t}/B_{\phi,t}\right) \approx \cos(\gamma)\, B_{\theta,t}/B_{\phi,t} \ , \tag{A.2}$$

where ξ refers to the direction perpendicular to the target surface as illustrated in the right part of Fig. A1. A mechanical misalignment $\Delta\xi$ of the tile in ξ direction must then be smaller than $\Delta\xi_{crit}$ with

$$2\Delta\xi_{crit} = w\tan\alpha - g\tan\theta_\perp, \tag{A.3}$$

or unscreened power flux is hitting the lateral surfaces of the tiles. Here the factor 2 is due to the worst case assumption that one tile is displaced by $-\Delta\xi_{crit}$ and the following by $+\Delta\xi_{crit}$. Obviously the condition

$$w\tan\alpha \geq g\tan\theta_\perp \tag{A.4}$$

must always hold since $\Delta\xi_{crit}$ cannot be negative. This is another design criterion for the divertor since α must be chosen sufficiently large not only for the envisaged standard operation of the device but for all phases in the discharge with possibly larger $\theta_\perp$ and significant power flux to the divertor.
Fig. A1 now shows that part of the tile is screened from the plasma, while only the

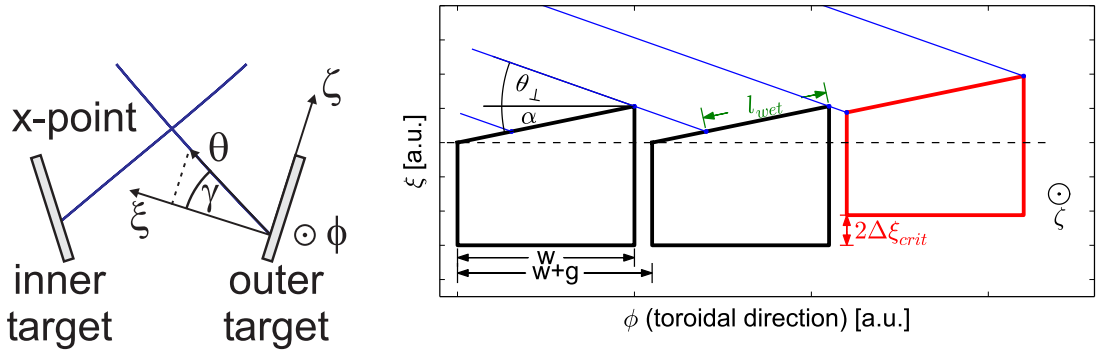

Figure A1. Divertor geometry

interval l_{wet} is exposed to it – at least, when assuming that the plasma is moving exclusively parallel to the magnetic field. The fraction of toroidally wetted area f_{TWA} (also 'toroidal wetted fraction') for heat flux is then given by

$$f_{TWA}\left(\alpha, \theta_{\perp}\right) = \frac{l_{wet}}{w+g} = \frac{\tan\theta_{\perp}}{\sin\alpha + \cos\alpha\tan\theta_{\perp}} \ , \tag{A.5}$$

which only depends on the angles α and $\theta_{\perp}$. As shown by Fig. A2 f_{TWA} becomes small, for small $\theta_{\perp}$ and a given α. For $\alpha \gtrsim 0.5^{o}$ for example $\theta_{\perp} \geq 2^{o}$ in order to keep $f_{TWA} \geq 80$ %. So from Eqs. A.1 and A.2 it is obvious that for given α, R_u, R_t and $B_{\theta,u}$ the magnetic flux expansion $f_{x,mag}$ and the target inclination angle γ can only increase the wetted area for power flux if

$$f_x = f_{x,mag}/\cos(\gamma) \leq \text{const.} \tag{A.6}$$

is fulfilled as mentioned in the introduction.

Note that this criterion may change significantly when taking into account finite gyro orbit effects and/or drifts. Furthermore the major radius of the machine is assumed to be large such that the radial coordinate R does not change significantly along the toroidal extension of the tile.

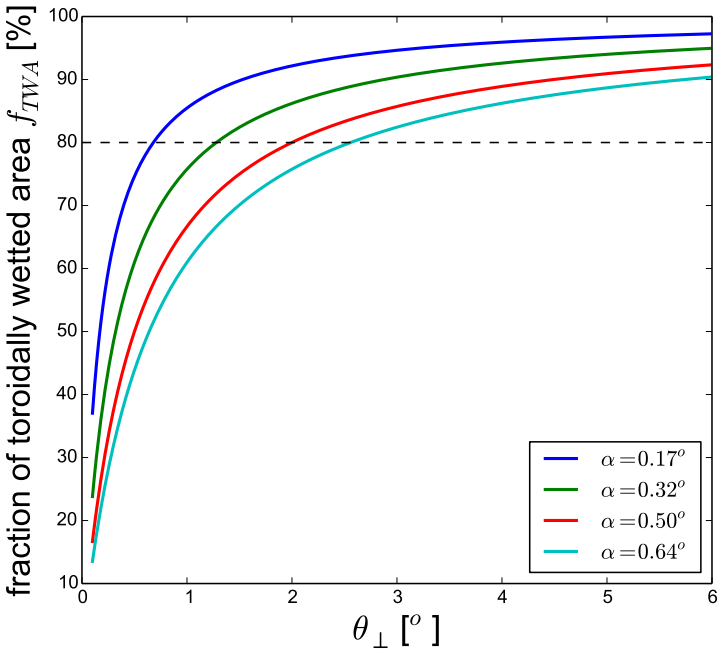

Figure A2. Fraction of toroidally wetted area as a function of the field line incidence angle $\theta_\perp$ for different toroidal inclination angles α (cf. Fig. A1).